

# Water entry of slender segmented projectile connected by spring

Zhengyang Wu<sup>a</sup>, Chengchun Zhang<sup>a,b,\*</sup>, Jing Wang<sup>c</sup>, Chun Shen<sup>b</sup>, Liang Yang<sup>d</sup>, Luquan Ren<sup>a</sup>

<sup>a</sup> Key Laboratory of Bionic Engineering (Ministry of Education), Jilin University, Changchun 130022, China

<sup>b</sup> State Key Laboratory of Automotive Simulation and Control, Jilin University, Changchun, 130022, China

<sup>c</sup> College of Physics, Jilin University, Changchun 130012, China

<sup>d</sup> Centre for Renewable Energy Systems, Cranfield University, Cranfield, MK43 0AL, United Kingdom

## Abstract

An object that enters the water experiences a large impact acceleration at the initial stage of water entry, which can cause structural damage to objects that are dropped or launched into the water. To reduce the peak impact acceleration, a spring-connected segmented projectile with compressible nose was designed. Through inertial measurement unit and high-speed camera, the influence of the nose compressibility on the initial impact acceleration was qualitatively investigated. The experimental results demonstrate that the introduction of a spring between the nose and the main body of the projectile can significantly suppresses the peak acceleration during the early stage of impact (0-50 ms). Furthermore, the maximum impact acceleration experienced by the main body is only related to the maximum compression of the nose without considering the spring stiffness. In addition, using the spring exerts a slight effect on the non-dimensional pinch-off times of the cavity but increases the initial velocity required for the occurrence of cavity pinch-off events on the side of the main body.

**Keywords:** segmented projectile, spring, water entry, impact acceleration reduction, cavity dynamics

## 1. Introduction

Studies of the water entry events of objects have been conducted for more than 100 years, and began with the first image of water droplets falling into a water-milk mixture photographed by Worthington and Cole (1897). This has been widely covered in different fields, including military applications such as missile water entry (May, 1975), civilian applications such as ship slamming (Tveitnes et al., 2008), aerospace engineering applications such as the design loads of spacecraft water entry (Hirano and Miura, 1970), and bio-specific functional mechanisms such as plunge-dive gannets

28 (Wang et al., 2013). The main research contents of water entry focus on the formation and evolution of  
29 the cavity (Lee et al., 1997; Bergmann et al., 2009; Duclaux et al., 2007), the trajectory of objects  
30 (Dupeux et al., 2010; Rosellini et al., 2005; Truscott and Techet, 2009), and the calculation of the  
31 impacting load (Korobkin and Pukhnachov, 1988; Korobkin and Scolan, 2006; Alaoui et al., 2015).  
32 This study presents an experimental study of the impact of a slender segmented projectile,  
33 spring-connected on a free surface. This study offers the first examination of how a compressible  
34 projectile nose affects the water-entry phenomenon, especially the impact force on the main body of  
35 the projectile.

36 In general, the water entry of objects can be divided into two categories: cavity forming and  
37 non-cavity forming. The major parameters that determine whether a cavity is formed include the  
38 capillary number  $Ca = \mu U_0 / \sigma$ , wetting angle, and geometry (Duez et al., 2007; Truscott and Techet,  
39 2009b). Furthermore, the larger the capillary number (high impact speed) and wetting angle, the more  
40 likely a cavity forms. The four typical types of cavities include surface seal, deep seal, shallow seal,  
41 and quasi-static seal (Aristoff et al., 2008; Aristoff and Bush, 2009) depending on the depth at which  
42 pinch-off occurs when a cavity forms. Among these types, the deep seal appears in most water entry  
43 cases and is characterized by the first pinch-off event, which occurs much closer to the sphere,  
44 typically at one-third to one-half of the distance between the sphere and the undisturbed free surface  
45 (Aristoff and Bush, 2009). To characterize the deep seal event, the important parameter of the  
46 non-dimensional pinch-off time,  $t^* = U_0 t / D$ , was used by Aristoff et al. (2010). Furthermore, the  
47 results show that the non-dimensional pinch-off times remain constant and independent of both impact  
48 velocity and mass ratio. Moreover, another non-dimensional pinch-off time,  $\tau = t \sqrt{2g / D}$ , was  
49 proposed by Glasheen and McMahon (1996) is used as well. Cavities with deep seal, which always  
50 form after water entry due to the slender geometric shape and the non-dimensional pinch-off times,  
51 were also examined in the present study.

52 The main source of the impact force during the initial stage of water entry is the added mass (Von  
53 Karman, 1929). Von Karman (1929) was the first to theoretically study the impact forces on seaplane  
54 floats during water entry and introduced the concept of added mass by assuming that the momentum of  
55 the water/body system is conserved. Wagner (1932) further developed the theory of Von Karman

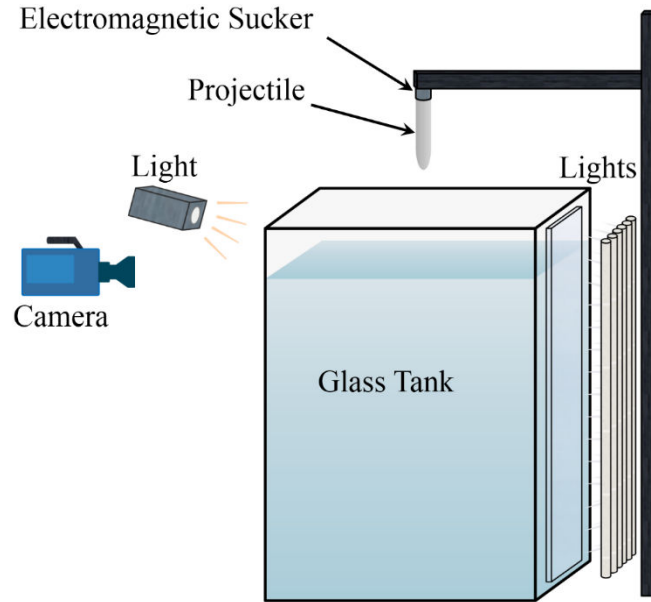
56 (1929) by considering the effects of the change in boundary conditions including the calculation of the  
57 piled-up water surface and the spray thickness. Subsequently, most theoretical studies (Yu, 1945;  
58 Shiffman and Spencer, 1951; Grady, 1979) on the impact force of water entry are based on their  
59 research. In addition to the added mass, the water hammer (Korobkin and Pukhnachov, 1988), which is  
60 generated at the sphere initially touches the water surface, is also one of the sources that contribute to  
61 the initial impact force. Furthermore, the formation of a high-speed radial jet greatly increases the  
62 initial impact force on the sphere as reported by Thoroddsen et al. (2004). Prior research (Shiffman and  
63 Spencer, 1945; Grady, 1979) on object impact on a water surface showed that a large peak acceleration  
64 exists during the very early stage of water entry. This may even appear at the time when the sphere is  
65 submerged between 10% and 20% of its radius (Moghisi and Squire, 1981).

66 To reduce the impact force, several studies have recently been conducted. Bodily et al. (2014)  
67 studied the effect of the nose shape of slender axisymmetric bodies on the peak impulsive force. The  
68 results showed that projectiles with cone-nose shape suffered the smallest impact force compared to  
69 other nose shapes. Chang et al. (2016) investigated the stability of the seabird's neck during  
70 plunge-diving. They simplified the bird system as a long, thin, elastic beam that is attached to a rigid  
71 cone, which represent the bird's neck and head, respectively. The result indicates that the axial force  
72 acting on the neck of the bird increases with the skull radius, especially the beak angle. Speirs et al.  
73 (2019) proposed a method to reduce the initial impact force experienced by a sphere during water  
74 impact by using a jet of water, which strikes the free surface prior to sphere impact. Introduction of this  
75 jet accelerates the previously static water and reduces the added mass effect on the impacting body.  
76 The force could be reduced by 75%, using this method.

77 It is self-evident that the appearance of the large impact force at the initial stage of entering water,  
78 as mentioned above, will cause both structural damage and internal component failure of objects. This  
79 study designed a segmented projectile with spring-connection with the primary aim to reduce the  
80 impact force. We expect that the peak force can be reduced by converting the kinetic energy induced  
81 by the impact of the free surface into potential energy of the spring. For quantitative analysis, to assess  
82 the influence of the introduction of spring on the initial impact force, an inertial measurement unit  
83 (IMU) was used to record the impact acceleration. Moreover, to study the cavity dynamics, a

84 high-speed camera was used to capture the impact event of the projectile during water entry. The  
85 experiment was carried out at a lower speed range and the water entry of a nose fixed projectile were  
86 used as comparative test.

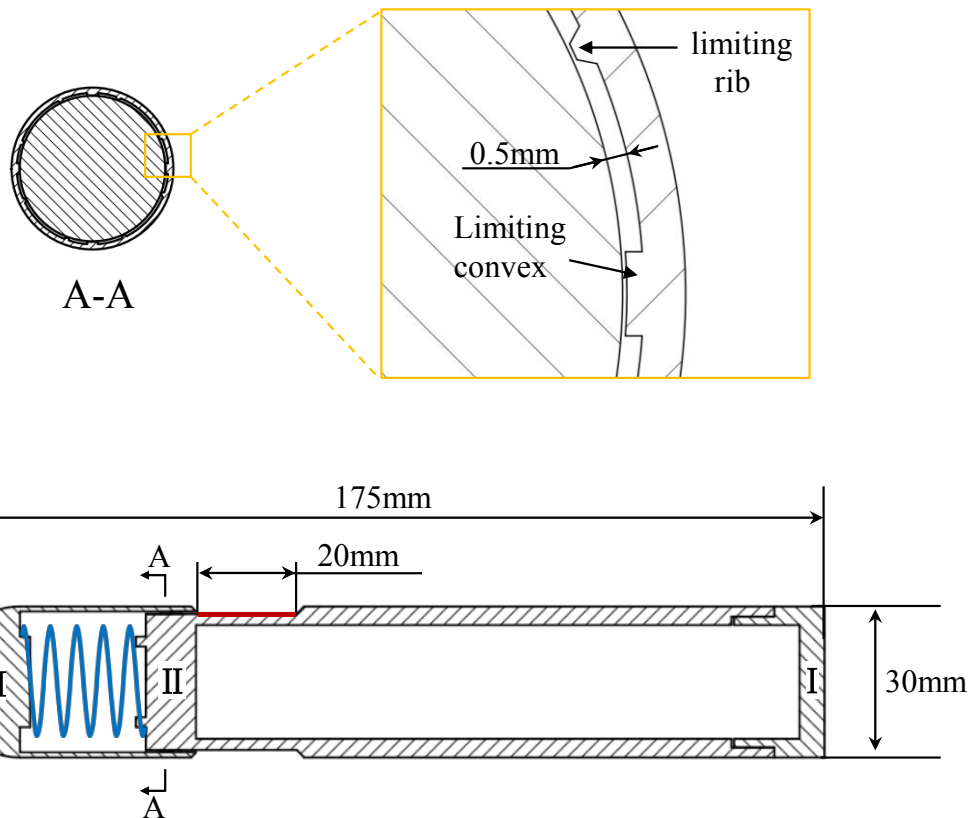
## 87 2. Experimental methods



88  
89 Fig. 1. Schematic view of the experimental apparatus.

90 Fig. 1 shows the experimental apparatus used for this study. The projectile was fixed on an  
91 electromagnetic sucker via iron sheet, which was stuck in the tail of the projectile. The initial impact  
92 velocity was controlled by varying the height between the tip of the nose of the projectile and the free  
93 surface. When the power of the electromagnetic sucker was interrupted, the projectile was released  
94 from the rest and fell freely toward the glass tank measuring  $70 \times 70 \times 100$  cm (width  $\times$  depth  $\times$  height)  
95 filled with water to 80 cm. Six different drop heights  $H_0$  were used to vary the initial impact velocity  
96 close to  $U_0 \approx \sqrt{2gH_0}$  by ignoring the air drag.  $U_0$  can also be determined through analysis of video  
97 sequences. A high-speed camera (Phantom V711, Vision Research, Inc.) that was positioned normal to  
98 the tank was utilized to capture the impact event of the projectile at a rate of 4000 frames/s with  $1280 \times$   
99  $800$  pixels. The conversion factor between mm and pixels is 0.526 mm/pixels. Six 36 W LED  
100 fluorescent tubes with a diffuser sheet were used to provide backlighting for the camera images and  
101 were placed behind the tank. A 1000W LED floodlight was used to provide the foreground lighting and

102 was placed in front of the tank.

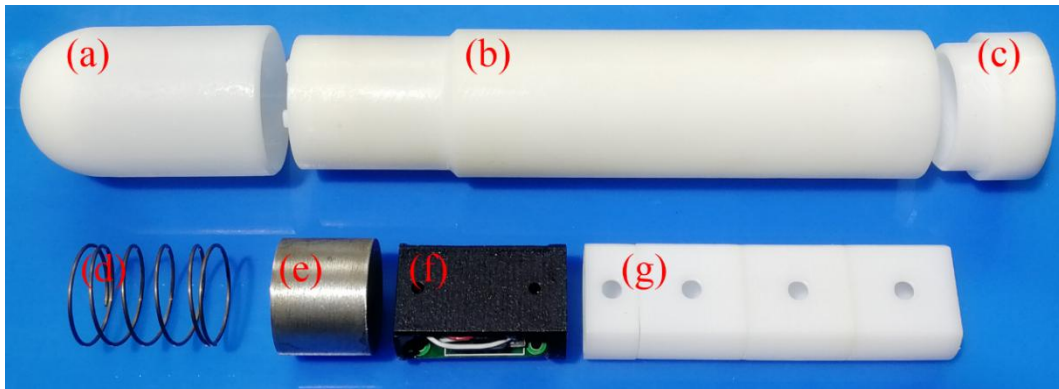


103

104 Fig. 2 Schematic diagram of geometric parameters of the projectile. A-A shows the section view and  
105 the yellow rectangular box shows a local enlargement.

106 To quantitatively analyze the influence of compressibility of the projectile nose on the water entry  
107 impact force and cavitation dynamics, a three-segment projectile including tail (I), main body (II), and  
108 nose (III) was designed, as shown in Fig. 2. The main body had a length of 125 mm and two outer  
109 diameters. The end with an outer diameter of 30 mm is connected to the tail and the other end with an  
110 outer diameter of 27 mm, which is connected to the nose. A cylindrical cavity with an inner diameter of  
111 22.6 mm and a length of 120 mm is formed after the main body and the tail are connected and is used to  
112 place the block weight, IMU, and spacers. The order of the block weight, IMU, and spacers is shown in  
113 Fig. 3. The block weight is placed at the bottom of the main body with the IMU is situated above. This  
114 moves the center of mass as close as possible to the nose of the projectile to minimize the projectile  
115 rotation and lateral displacement during water entry (Bodily et al., 2014). The nose of the projectile has  
116 a hemispheric nose shape with an outer diameter of 30 mm, an inner diameter of 28 mm, and a length  
117 of 50 mm. Eight limiting ribs were uniformly arranged on the inner-wall of the nose to ensure that the

118 nose moves only along the axis of the main body when assembled. Four limiting convexes were  
 119 uniformly arranged on the inner-wall of the nose and the outer-wall of the main body, to limit the  
 120 position between them and to ensure that the nose does not slip from the projectile during testing. The  
 121 gap between the limiting rib and the outer-wall of the main body was 0.05 mm, which ensures high  
 122 axiality. A spring with a 20 mm maximum compression length was installed between the nose and the  
 123 main body, which is also the maximum sliding length (marked with the red line in Fig. 2) of the nose  
 124 along the main body. The main parameters of the spring are listed in Table 1. The projectile used in this  
 125 study was made by 3D printing technology using UV Curable Resin. This provides a hydrophilic  
 126 surface with a wetting angle  $\theta = 79 \pm 5^\circ$  and surface roughness  $R_z = 7.8 \pm 1.2 \mu\text{m}$ .



127  
 128 Fig. 3 Physical splitting chart of the projectile. (a) Nose. (b) Main body. (c) Tail. (d) Spring. (e) Block  
 129 weight. (f) Inertial measurement unit (IMU). (g) Spacers.

130 The IMU has a three-axis accelerometer and was used to record the instantaneous acceleration that  
 131 the projectile experienced during water entry at a rate of 2000 Hz. The accelerometer is an ICM42605  
 132 motion tracking device manufactured by InvenSense Inc. and was set to a maximum range of  $\pm 16 \text{ g}$   
 133 with a measurement error of 0.01 g.

134 Table 1. The main parameters of the spring

Material	Stiffness (N/mm)	Line diameter (mm)	Outer diameter (mm)	Free length (mm)
Stainless steel	0.1	0.8	19.6	25

135 Two forms of projectiles were used in this study. For the first form, the nose was fixed on the main  
 136 body through a sealant, which avoided the relative displacement between the nose and the main body  
 137 during the test. This form was called Nose Fixed Projectile (NFP). For the second form, the nose and

138 the main body are not fixed. During the initial stage of impact, the nose is decelerated by a large  
 139 hydraulic impact pressure, while the main body continues to accelerate while falling due to its large  
 140 inertia. Relative motion occurs between them, which results in axial compression of the spring. It can  
 141 be considered that the nose is compressed relative to the main body. This form was called Nose  
 142 Compressible Projectile (NCP). Both forms of projectile have the same total length of  $L = 175$  mm and  
 143 density of  $\rho = 1.12$  g/cm<sup>3</sup> before impacting the free surface.

144 Table 2. Initial water entry initial condition for the projectile

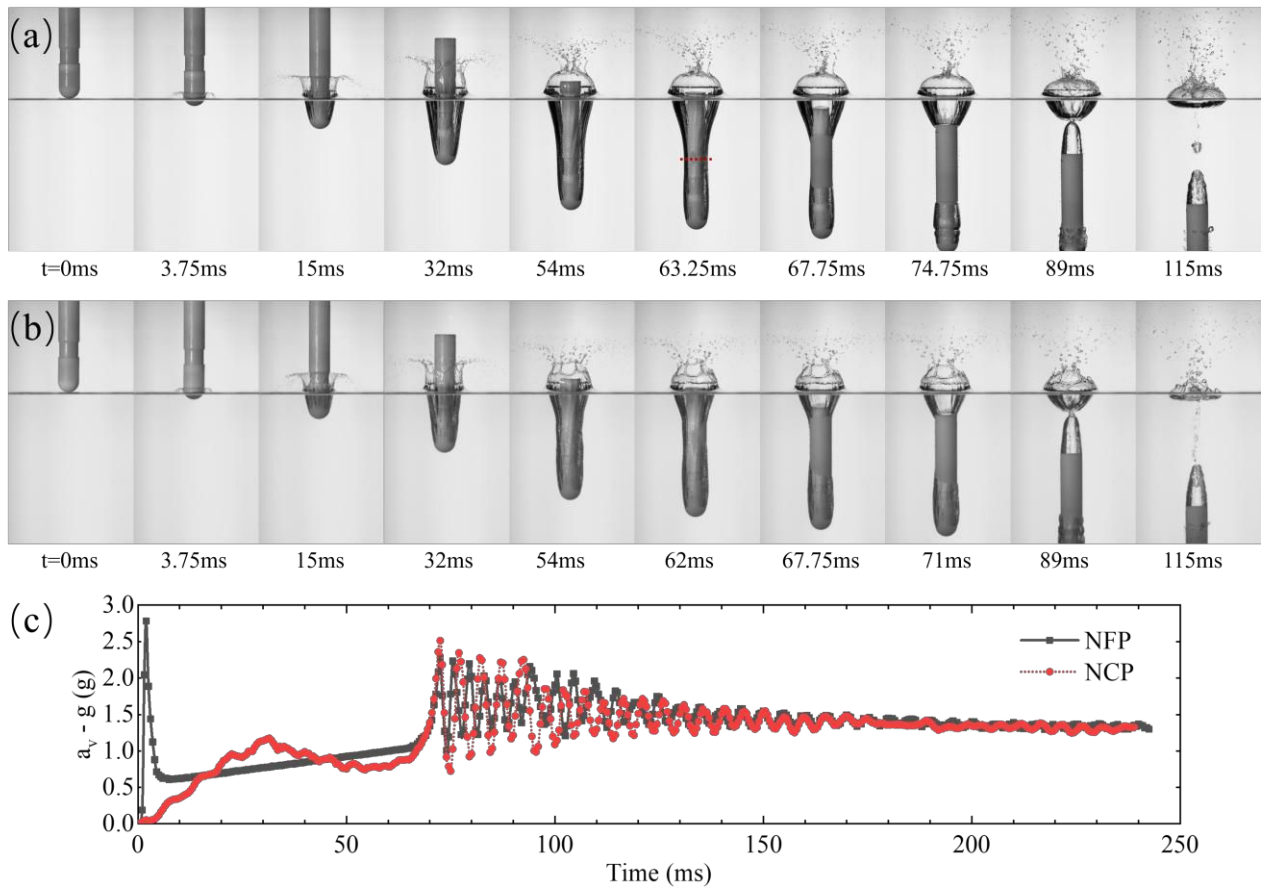
$H_0$ (m)	$U_0$ (m/s)	Reynolds	Weber	Froude
0.1	1.40	46879	814	2.58
0.2	1.98	66296	1628	3.65
0.3	2.43	81196	2442	4.47
0.4	2.80	93757	3256	5.16
0.6	3.43	114829	4884	6.32
0.8	3.96	132593	6511	7.30

145 In this study, three non-dimensional parameters, Reynolds number  $Re = \rho_w U_0 D / \mu$ , Weber  
 146 number  $We = \rho_w U_0^2 D / \sigma$ , and Froude number  $Fr = U_0 / \sqrt{gD}$  were used to characterize the water  
 147 entry of the projectile. Here,  $\rho_w$  represents the water density,  $D$  represents the radius of the projectile,  $\mu$   
 148 represents the dynamic viscosity of the water,  $\sigma$  represents the surface tension, and  $g$  represents the  
 149 acceleration due to gravity. The parameters used in this study are listed in Table 2.

150 At least five effective tests were conducted at each height for each form of projectile. The  
 151 compression of the nose relative to the main body during water entry of NCP, which is also a spring  
 152 compression, was measured in pixels from the recorded images, and the uncertainty of measurement  
 153 from the pictures is  $\pm 1$  pixel (corresponding to  $\pm 0.5$  mm). All tests were conducted at atmospheric  
 154 pressure and room temperature (about 25 °C).

155 **3. Results and discussion**

156 **3.1. Cavity dynamics and projectile acceleration**



157  
158 **Fig. 4** Image sequence of water entry and corresponding axial impact acceleration. (a) NFP impacts  
159 free surface at a velocity of  $U_0 = 2.80$  m/s. (b) NCP impacts free surface at the same velocity of  $U_0 =$   
160  $2.80$  m/s. (c) **The axial impact acceleration  $a_v - g$ , normalized by  $g$  versus time for NFP and NCP**  
161 **impacting the free surface in (a) and (b).**

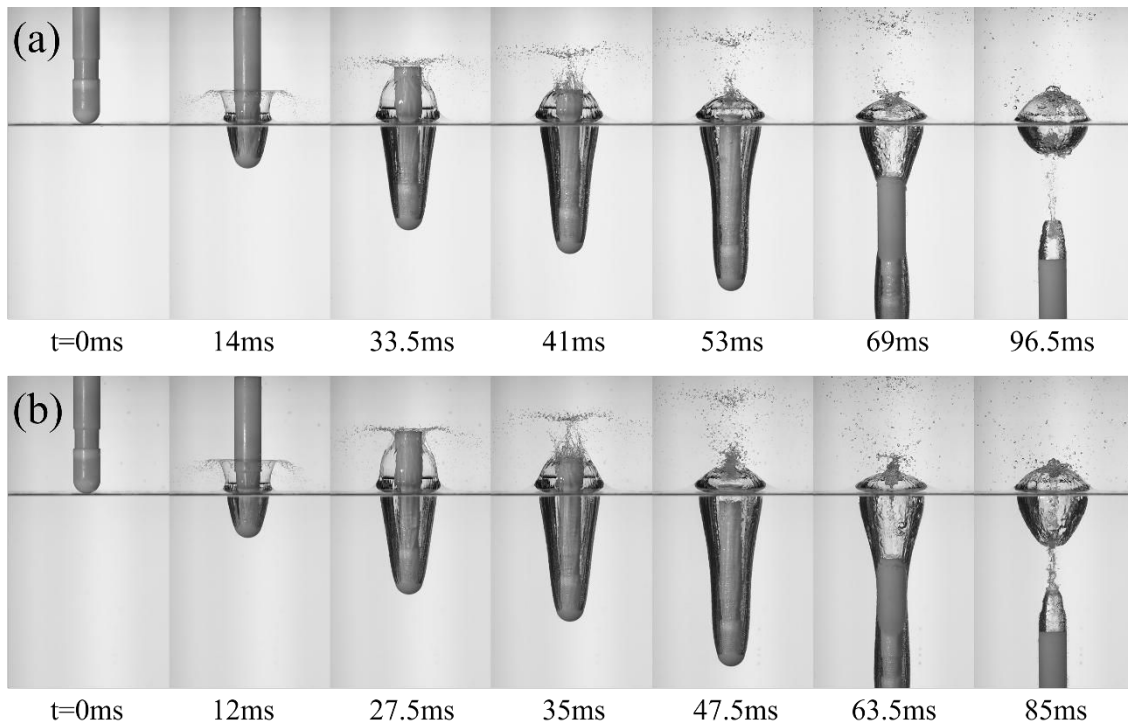
162 Fig. 4(a) and (b) show the image sequence of the NFP and NCP impacting the free surface at the  
163 same initial velocity of  $U_0 = 2.80$  m/s. Fig. 4(c) shows the corresponding axial impact acceleration,  
164 normalized by  $g$ , **where the axial impact acceleration is the real acceleration  $a_v$ , minus the gravity  $g$ .**  
165 For the NFP water entry, an initial horizontal jet of fluid forms as the projectile impacts the free surface,  
166 followed by the formation of a vertical splash crown as the nose of the projectile penetrates the water.  
167 With decreasing air pressure in the cavity, the splash crown moves inward. At the time of 54 ms, a  
168 surface closure occurs behind the tail of the projectile. However, in the test of higher initial velocity  
169 ( $U_0 = 3.43$  m/s and 3.96 m/s), the surface closure appears first on the side of the projectile and then



170 again on the tail, as shown in Fig. 5. At 63.25 ms, a deep seal of the main cavity occurs on the side of  
171 the projectile, generating a three-phase contact line of the air-water-projectile. Then, the contact line is  
172 divided into two and moves fast in the opposite direction along the side of the projectile with the main  
173 cavity split into two separate cavities. The lower cavity remains attached to the forehead of the  
174 projectile when the contact line moves to the shoulder of the main body and oscillates as the projectile  
175 enters deep into the water. At the same time, another contact line moves quickly to the tail of the  
176 projectile and is attached to the edge of the tail. At the time of  $\sim 89$  ms, the second-deep seal happened  
177 with the upper cavity pinch-off behind the tail of the projectile. Two separate cavities generate again,  
178 where the upper cavity is connected to the free surface and the lower cavity is attached to the tail of the  
179 projectile. Ripples in the tail cavity are seen similar to when a sphere enters the water as described by  
180 Grumstrup et al. (2007). Then, vortex shedding begins and a bubble separates from the tail cavity and  
181 rises to the water surface. The black dotted line shows the corresponding NFP axial impact  
182 acceleration curve versus time. During the very early stages of impact (0-10 ms) an acceleration spike  
183 appears first due to the nose of the projectile accelerating a portion of the surrounding water (added  
184 mass) (Shiffman and Spencer, 1945). A linear increase of the acceleration followed until about the time  
185 of 63.25 ms, when the pinch-off of the main cavity occurred on the side of the projectile. Then, the  
186 acceleration increased sharply and another peak of the acceleration appeared at the time of  $\sim 74.75$  ms,  
187 which is the moment when the contact line moves to the edge of the tail. During this time (63.25-74.75  
188 ms), the main cavity collapses on the side of the projectile. The contact area between the fluid and the  
189 projectile increases, resulting in the increase of viscous drags and differential pressure drags of the  
190 fluid on the projectile. Then, a periodic acceleration oscillation appears, which is caused by the  
191 disturbance of the surrounding fluid due to the collapse of the upper cavity and the oscillation of the  
192 tail cavity.

193 When NCP enters the water, compared with NFP a weaker jet of fluid, followed by a smaller cavity,  
194 formed at the initial stage of impact. Compression begins between the nose and the main body, which  
195 are connected by a linear spring. At the time of  $\sim 32$  ms, the compression of the nose achieved  
196 maximum ( $\sim 11.86$  mm). At the time of 62 ms, pinch-off occurs on the side of the projectile. The  
197 subsequent evolution trend of the cavity is basically identical to that of NFP. Throughout the water

198 entry process, the size of the cavity formed by NCP entering water is clearly smaller than that of NFP  
 199 and the splash crown remains open without forming a dome. The red dotted line is the corresponding  
 200 NCP axial impact acceleration curve versus time. This acceleration is the measured value of the main  
 201 body of the projectile. Compared to the acceleration curve of NFP, the acceleration spike disappeared  
 202 during the very early stages of impact and were replaced by a gradually increasing acceleration from 0  
 203 ms to about 32 ms. Then, a slight decline in acceleration occurred, followed by a sharp increase in  
 204 acceleration at ~62 ms. A peak of the acceleration appeared at the time of ~71 ms, which is also the  
 205 moment when the contact line moves to the edge of the tail. The subsequent variation trend and  
 206 magnitude of acceleration are basically consistent with those of NFP. As the use of the spring between  
 207 the nose and the main body of the projectile significantly suppressed the peak impact acceleration  
 208 during the early stage of impact (0-50 ms) and exerted little effect on the subsequent acceleration, the  
 209 following mainly focused on this period of the impact.

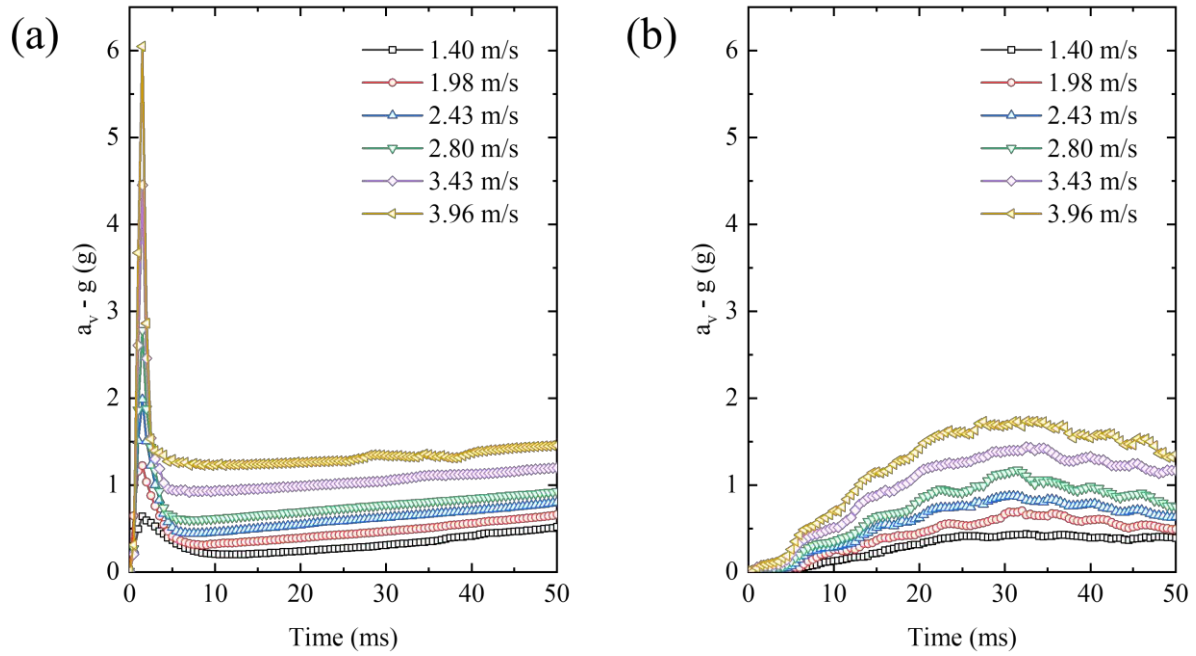


210  
 211 Fig. 5 Image sequence of water entry for NFP. (a)  $U_0 = 3.43$  m/s, the surface closure appears first on the  
 212 side of the projectile at the time of 33.5ms and then again on the tail at the time of 53ms. (b)  $U_0 = 3.96$   
 213 m/s, the surface closure appears first on the side of the projectile at the time of 27.5ms and then again  
 214 on the tail at the time of 47.5ms.

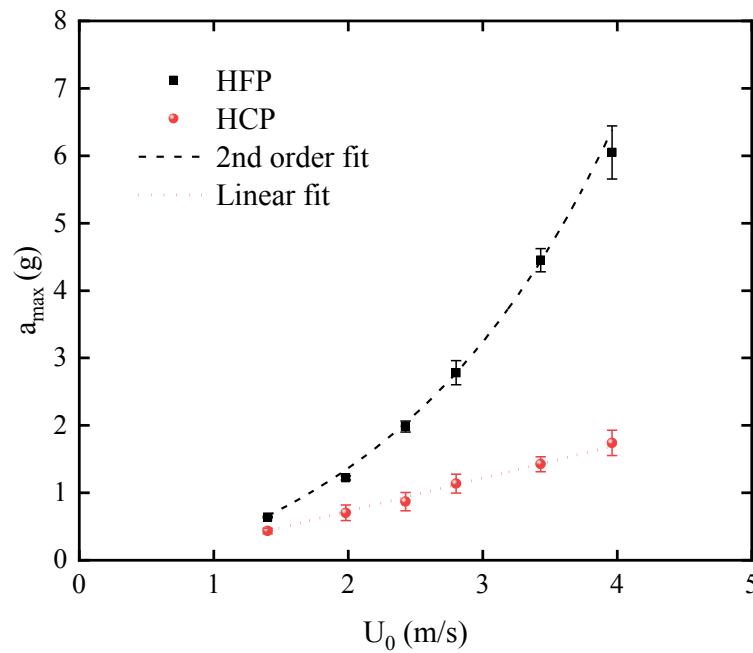
### 215 3.2. Effects of the initial velocity on the impact acceleration of projectile

216 Fig. 6(a) and (b) show the axial impact acceleration, normalized by  $g$ , as experienced by both  
217 projectiles (NFP and NCP) during the early stage of impact under the conditions of six different initial  
218 velocities. In order to measure the peak impact acceleration more accurately, at least 5 effective tests  
219 have been carried out at each height for NFP and NCP. Here, the effective test refers to the test that  
220 the projectile does not rotation and lateral displacement during water entry. The data used in Fig. 6  
221 are the mean values of five effective tests. For the NFP impacting water, two stages of impact  
222 acceleration could be separated. The first stage was 0-10 ms, when the peak acceleration occurred at  
223  $\sim 1.5$  ms and the relationship between the maximum acceleration  $a_{max}$  normalized by  $g$  and the initial  
224 impacting velocity  $U_0$  is quadratic. Therefore, a second-order curve can be used to fit the variation of  
225  $a_{max}/g$  with  $U_0$  as shown in Fig. 7, where the error bars represent the standard deviation which is also  
226 used in other graphs in this paper. **To be clear, due to the sampling rate is not high enough, the timing  
227 and magnitude of peak acceleration shown in Fig. 6 may not reflect the true peak.** The second stage is  
228 10-50 ms, and the acceleration increases linearly with approximately the same growth rate at different  
229 initial velocity. At the moment of 30 ms, the axial acceleration was plotted as a function of  $U_0$  in Fig. 8  
230 to show the relationship between them during the second stage. A linear curve was found to fit them  
231 well. When the NCP impacts water, no peak impact acceleration appeared in all initial impact velocity  
232 tests. Within the time of about 0-5 ms, a small increase in acceleration can be seen. Then, within 5-20  
233 ms, the acceleration increased approximately linearly. Next, the acceleration started to slow down at  
234 the period of 20-32 ms. At the time of  $\sim 32$  ms, the acceleration reached its maximum and the time it  
235 took for the NCP entry water to reach the maximum acceleration is basically independent of the initial  
236 impact velocity  $U_0$ . A slight decrease in acceleration occurred within 30-50 ms except for the test of  $U_0$   
237  $= 1.40$  m/s. It should be noted that the acceleration curve is not smooth for the NCP entry water, but has  
238 slight fluctuation. The main reason is that a tiny but discontinuous friction force is generated between  
239 the nose and the main body when it is compressed, which acts on the main body, resulting in the  
240 fluctuation of acceleration during water entry. In comparison, the maximum impact acceleration  $a_{max}$   
241 normalized by  $g$  experienced by NCP in the initial stage of impact is also plotted in Fig. 7. The  
242 relationship between  $a_{max}/g$  and  $U_0$  is linear for the NCP impact. Moreover, the difference of maximum

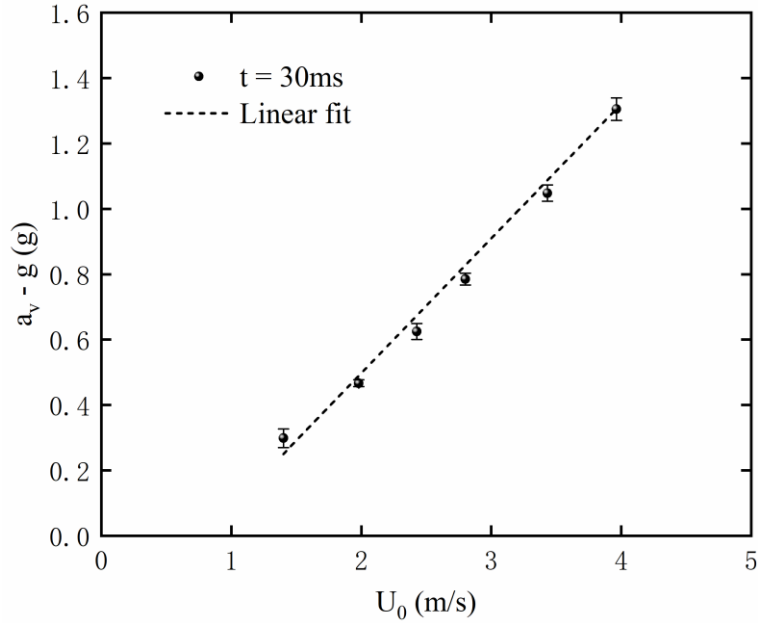
243 impact acceleration between both projectiles increased significantly with increasing initial velocity  $U_0$ .  
 244 This shows that the effect of the spring on the reduction of the maximum impact acceleration of the  
 245 high-speed projectile is stronger during the early stage of impact.



246  
 247 **Fig. 6** Time history of the axial impact acceleration, normalized by g under the conditions of six  
 248 different initial velocities. (a) NFP impacts free surface. (b) NCP impacts free surface.



249  
 250 **Fig. 7** Maximum acceleration  $a_{max}$ , normalized by g as a function of the initial velocity  $U_0$  for NFP and  
 251 NCP during the initial stage of impact.



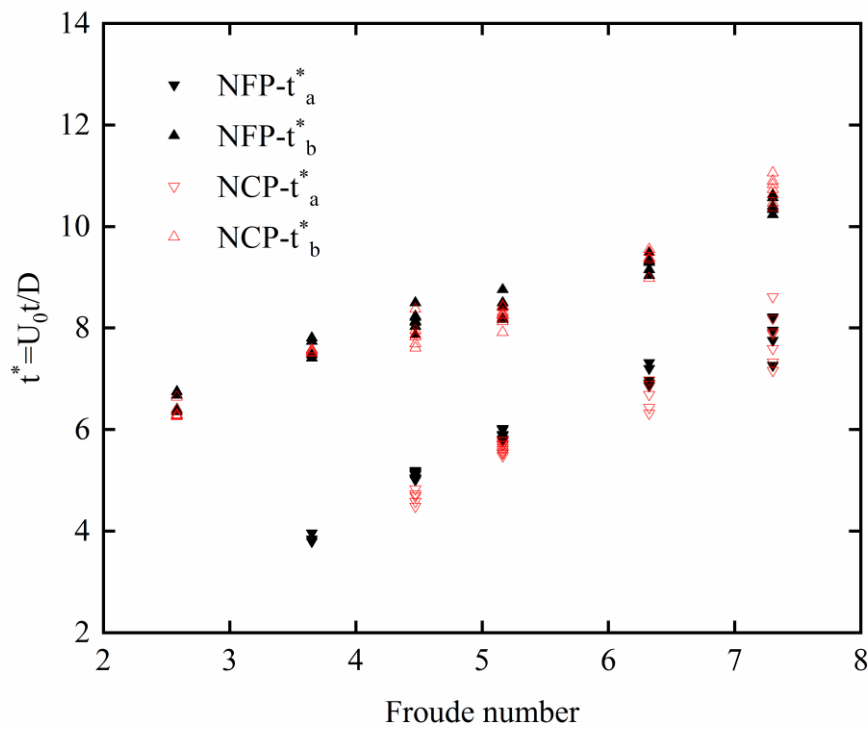
252

253 **Fig. 8** Axial impact acceleration, normalized by  $g$  as a function of the initial velocity  $U_0$  for NFP at the  
 254 moment of 30 ms.

255 **3.3. Cavity pinch-off**

256 As mentioned in Section 3.1, two deep seals occur at the impacting event of  $U_0 = 2.80$  m/s, one of  
 257 which occurs on the side of the projectile and the other occurs behind the tail of the projectile. Clearly,  
 258 the deep seal occurring on the side of the projectile greatly influence the formation and development of  
 259 the second peak acceleration. Furthermore, the occurrence of deep seal behavior on the side of the  
 260 projectile may also exert an effect on the initial impact acceleration. Therefore, the non-dimensional  
 261 pinch-off times ( $t^* = U_0 t / D$ ) for both forms of projectiles were used to characterize the two deep seal  
 262 events. Figure 9 shows the relationship between the non-dimensional pinch-off time  $t_a^*$  and  $t_b^*$   
 263 versus the Froude number, where  $t_a^*$  represents the non-dimensional time of the main cavity  
 264 pinch-off on the side of the projectile, and  $t_b^*$  represents the non-dimensional time of pinch-off  
 265 behind the tail of the projectile. The used of the spring between the nose and the main body of the  
 266 projectile slightly affected the non-dimensional pinch-off times  $t_a^*$  and  $t_b^*$ . Furthermore, the  
 267 non-dimensional pinch-off time  $t_a^*$  increased linearly with the Froude number; however, there is no  
 268 clear relationship between  $t_b^*$  and the Froude number. The single value of dimensionless pinch-off

269 time,  $\tau = t\sqrt{2g/D}$ , was also calculated. The values for NFP and NCP pinch-off on the side of the  
 270 projectile were  $\tau_{a-NFP} = 1.573 \pm 0.0621$  and  $\tau_{a-NCP} = 1.513 \pm 0.0628$ , which are almost equal to the  
 271 value of  $\tau_A = 1.530 \pm 0.155$  as reported for a cone nose shape projectile by Bodily et al. (2014).  
 272 Moreover, at the velocity of  $U_0 = 1.98$  m/s, no pinch-off events occurred on the side of the projectile for  
 273 NCP entry water. This is because the deformation of spring absorbed the partial inertia, which is  
 274 required by the nose cavity forms. Therefore, the use of spring increased the initial velocity required  
 275 for the occurrence of pinch-off behavior on the side of the projectile.

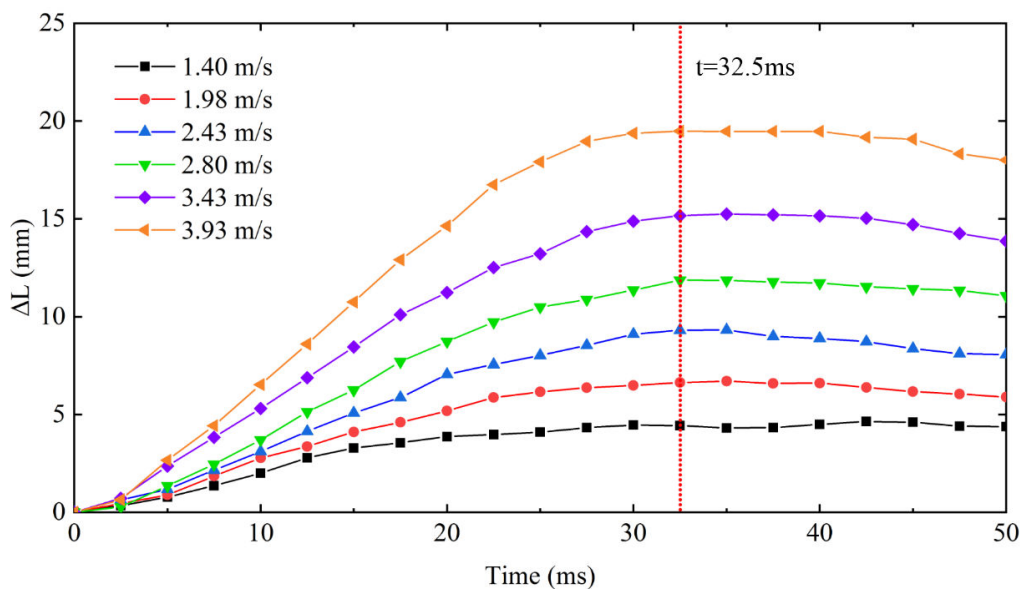


276  
 277 Fig. 9 Non-dimensional pinch-off time as a function of the Froude number for NFP and NCP.

278 **3.4. Compression of the nose for NCP**

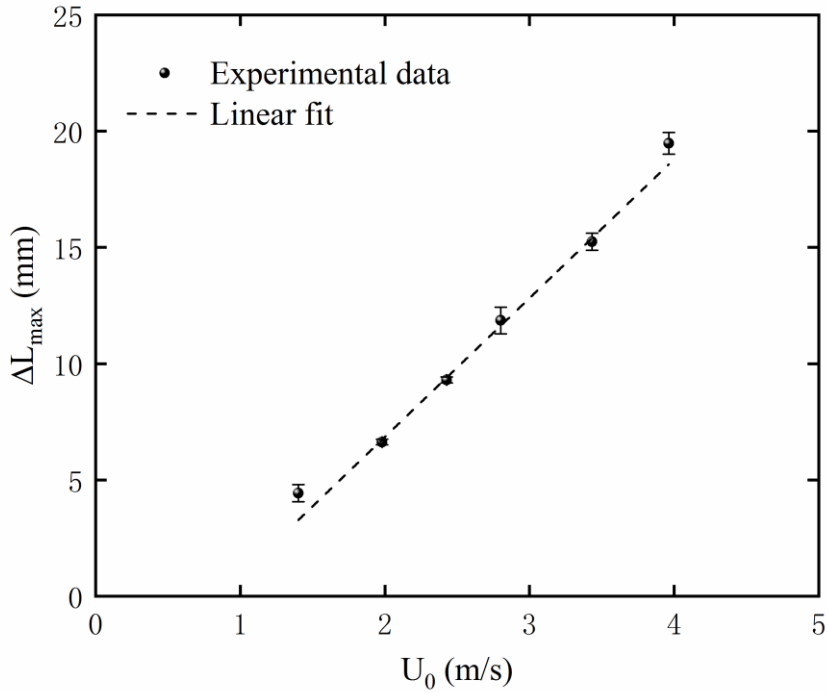
279 The most intuitive phenomenon corresponding to the reduction of the maximum acceleration of the  
 280 NCP during the early stage of impact is the compression of the nose. Fig. 10 shows the time history of  
 281 the amount of nose compression ( $\Delta L$ ) for NCP during the early stage of impact under the conditions of  
 282 different initial velocities.  $\Delta L$  is also the amount of spring deformation. At the beginning of 2.5 ms, the  
 283 compression of the nose is small. Within the time of  $\sim 2.5$ -20 ms, the nose compression increased

284 approximately linearly and then slowed down until it reached its maximum at about 32.5 ms. Finally,  
 285 the compression decreased slightly after remaining constant for a period of time. However, it should  
 286 be noted that the compression may have reached the maximum compression length (20 mm) of the  
 287 spring between approximately 30-40 ms at the velocity of  $U_0 = 3.93$  m/s due to potential combined  
 288 manufacturing tolerances and deflection measurement accuracy, although the compression measured  
 289 by us is less than 20 mm. The variation trend of the nose compression with time at different initial  
 290 velocities is basically identical to that of the impact acceleration experienced by the NCP during the  
 291 early stage of impact when entering the water. Furthermore, the time when the amount of the nose  
 292 compression reached its maximum value  $\Delta L_{\max}$  basically remained the same as the time when the  
 293 impact acceleration reached its maximum value. The slight time difference could be attributed to the  
 294 lack of the sampling data of compression at the time of 32 ms. Fig. 11 shows the relationship of the  
 295 maximum compression  $\Delta L_{\max}$  and the initial velocity  $U_0$ . The maximum compression increased  
 296 linearly with increasing initial velocity. Fig. 12 shows the instantaneous water entry events of NCP  
 297 with different initial velocities at a time of 32.5 ms. At the low speed (1.40 m/s and 1.98 m/s), although  
 298 no cavity appeared in the nose of the projectile, the water did not touch the main body of the projectile  
 299 due to the low depth of penetration. At relatively high initial velocities, there is also no contact  
 300 between the water and the main body due to the formation of the cavity. This significantly simplified  
 301 the analysis of the force that acts on the main body of the projectile during the early stage of impact.

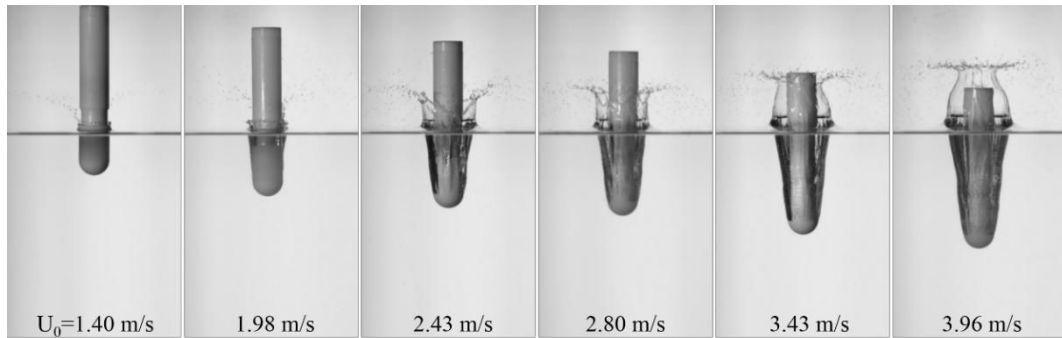


302

303 Fig. 10 Time history of the amount of nose compression  $\Delta L$  for NCP under the conditions of six  
 304 different initial velocities. The red dotted line indicates the time required to reach the maximum  
 305 compression.



306  
 307 Fig. 11 Maximum compression  $\Delta L_{max}$  as a function of the initial velocity  $U_0$  for NCP during the initial  
 308 stage of impact.



309  
 310 Fig. 12 Instantaneous water entry events of NCP with different initial velocities at the time of 32.5 ms

### 311 3.5. Force acting on the main body of NCP

312 To further understand the reason for the reduction of the maximum impact acceleration of NCP  
 313 during the early stage of impact, a force analysis of the main body is presented in the following. As  
 314 mentioned in Section 3.3, the pinch-off time of the cavity on the side of NCP was  $\sim 62$  ms, which is



315 almost not affected by the compression of the nose and beyond the time range discussed. Even in low  
 316 speed impact events, where no pinch-off occurs in the side of main body, no contact happened between  
 317 the main body and the water before the nose reached maximum compression. Therefore, the forces  
 318 acting on the main body can be shown in Fig. 13. A vertical force balance on the main body may be  
 319 expressed as

$$320 \quad m_b a = F_s + F_d + F_f - m_b g \quad (1)$$

321 where  $m_b$  represents the mass of the main body of projectile,  $a$  represents the absolute acceleration of  
 322 the main body,  $F_s$  represents the force of spring acting on the main body,  $F_d$  represents the air drag, and  
 323  $F_f$  represents the frictional force between nose and main body. Ignoring the air drag  $F_d$  and assuming a  
 324 very small friction  $F_f$  between the nose and the main body (which was considered at the beginning of  
 325 the design to reduce this friction between them), Equation (1) can be simplified to:

$$326 \quad m_b (a + g) = F_s \quad (2)$$

327 The force  $F_s$  is not clear in the process of the nose compression because the nose is not stationary and  
 328 moving relative to the main body. Fortunately, the maximum impact acceleration experienced by the  
 329 main body and the maximum compression of the nose appear almost at the same time and the  
 330 compression remained constant a short time after reaching the maximum compression in all conducted  
 331 tests. Therefore, a consistent motion state of the nose and the main body occurred and the force of  
 332 spring acting on the main body  $F_s$  was thus equivalent to the force required to deform the spring, i.e.,  
 333  $F_s = \Delta L_{\max} \cdot K$ , where  $\Delta L_{\max}$  represents the maximum deformation of spring at different velocities and  
 334  $K$  represents the spring stiffness. Non-dimensionalizing Equation (2), the maximum impact  
 335 acceleration  $a_{\max}$  can be predict by:

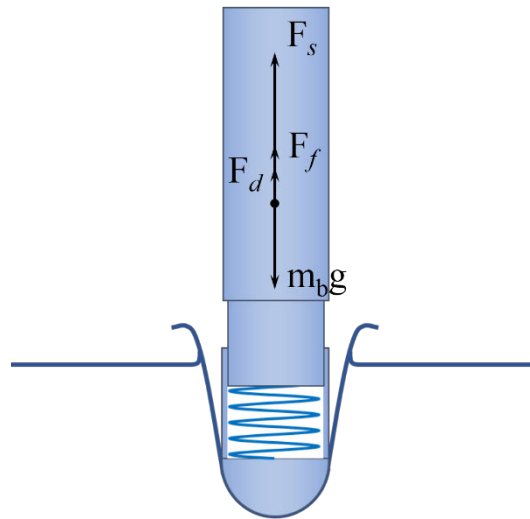
$$336 \quad \frac{a_{\max}}{g} = \frac{K \cdot \Delta L_{\max}}{m_b g} \quad (3)$$

337 where  $a_{\max}$  is the measured value of maximum acceleration, and the relationship between absolute  
 338 value and measured value is the absolute acceleration is equal to the measured acceleration minus the  
 339 gravitational acceleration  $g$ , thus, here have:

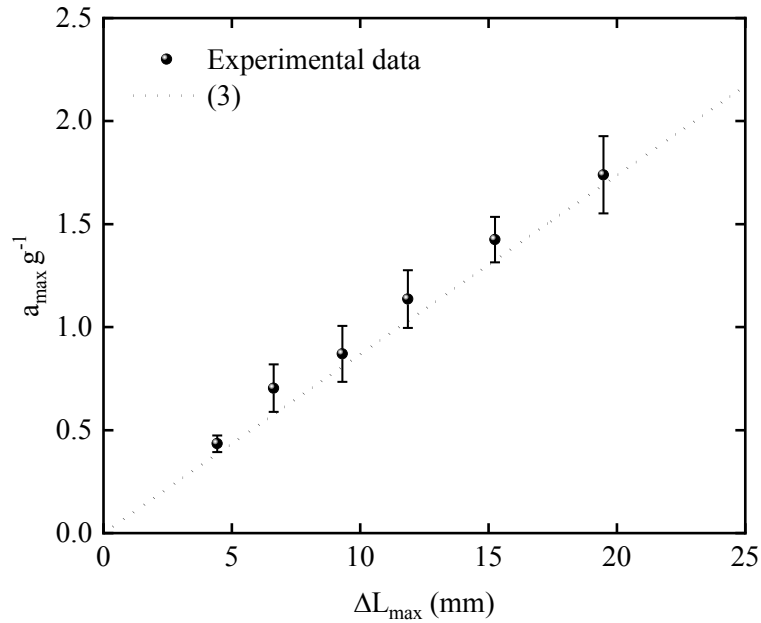
$$340 \quad a_{\max} = a_{\text{amax}} - g \quad (4)$$

341 where  $a_{\max}$  is the maximum absolute acceleration.  
342 The maximum measured acceleration  $a_{\max}$  was normalized by  $g$  and plotted as a function of  $\Delta L_{\max}$  in  
343 Fig. 14. The dotted line indicates the prediction Equation (3). The experimental results basically  
344 coincide with theoretical predictions.

345 At the initial stage of water entry, the larger fluid force acts on the projectile in a short time,  
346 producing a large impulse and then resulting in a peak acceleration. When the spring is introduced  
347 between the nose and the main body, although the nose will suffer a large impact force, the  
348 deformation of the spring absorbs part of the impulse, thus reducing the peak value of the impact  
349 acceleration and delaying the occurrence time of the maximum impact acceleration. The larger initial  
350 impact force is transferred to the finite spring deformation in the form of energy conversion. Thus,  
351 the using of the spring can effectively reduce the peak acceleration during the early stage of impact.



352  
353 Fig. 13 Schematic diagram of force acting on the main body of the projectile during the initial stage of  
354 water entry.



355

356 Fig. 14 Maximum impact acceleration  $a_{\max}$  as a function of the maximum deformation  $\Delta L_{\max}$  for NCP  
 357 during the initial stage of impact.

358

#### 359 4. Conclusion

360 Water entry tests of two forms of slender projectiles were performed in this study. A peak impact  
 361 acceleration for the nose fixed projectile (NFP) was found during the initial stage of water entry. The  
 362 experimental results show that the maximum impact acceleration experienced by the NFP increased  
 363 quadratically with the initial impact velocity during the early stage of impact. When a spring is  
 364 introduced between the nose and the main body (NCP), the maximum impact acceleration increases  
 365 linearly with the initial impact velocity and is significantly reduced at a relatively high initial velocity.  
 366 For NCP, the time until the maximum impact acceleration is reached is  $\sim 32$  ms, independent of the  
 367 initial impact velocity. The time required for the nose to achieve maximum compression is also  
 368 independent of the initial impact velocity and consistent with the maximum impact acceleration. The  
 369 maximum compression increases linearly with increasing initial velocity. In addition, the nose  
 370 compression spring increases the initial velocity required for the occurrence of cavity pinch-off events  
 371 on the side of the main body. However, it slightly affects the non-dimensional pinch-off times of the  
 372 cavity on the side of main body and the tail of the projectile. Finally, a simple prediction formula is  
 373 established to indicate the relationship between the maximum impact acceleration and the maximum

374 nose compression. Compared to the test results, the maximum impact acceleration of the main body is  
375 only related to the maximum compression of the nose under the same spring stiffness. Since the  
376 deformation of the spring absorbs part of the impulse, thus decreasing the peak value of the impact  
377 acceleration and delaying the occurrence time of the maximum impact acceleration. This explained  
378 why the maximum impact acceleration can be effectively suppressed during the initial stage for NCP.  
379 This study has significant practical value for the design of objects to reduce the impact force they are  
380 exposed to during water entry.

### 381 **Acknowledgements**

382 This study was supported by the National Key Research and Development Program of China  
383 (Grant No. 2018YFA0703302), the National Natural Science Foundation of China (Grant No.  
384 51575227, 51875243, 51706084), the Science and Technology Development Program of Jilin  
385 Province (Grant No.20180101319JC).

### 386 **References**

- 387 Alaoui, A.E., Nême, A., Scolan, Y.M., 2015. Experimental investigation of hydrodynamic loads and  
388 pressure distribution during a pyramid water entry. *J. Fluids Struct.* 54, 925–935.
- 389 Aristoff, J.M., Bush, J.W.M., 2009. Water entry of small hydrophobic spheres. *J. Fluid Mech.* 619,  
390 45–78.
- 391 Aristoff, J.M., Truscott, T.T., Techet, A.H., Bush, J.W.M., 2010. The water entry of decelerating  
392 spheres. *Phys. Fluids* 22, 1–8.
- 393 Aristoff, J.M., Truscott, T.T., Techet, A.H., Bush, J.W.M., 2008. The water-entry cavity formed by  
394 low Bond number impacts. *Phys. Fluids* 20, 091111.
- 395 Bergmann, R., van der Meer, D., Gekle, S., van der Bos, A., Lohse, D., 2009. Controlled impact of a  
396 disk on a water surface: Cavity dynamics. *J. Fluid Mech.* 633, 381–409.
- 397 Bodily, K.G., Carlson, S.J., Truscott, T.T., 2014. The water entry of slender axisymmetric bodies.  
398 *Phys. Fluids* 26, 072108.
- 399 Chang, B., Croson, M., Straker, L., Gart, S., Dove, C., Gerwin, J., Jung, S., 2016. How seabirds  
400 plunge-dive without injuries. *Proc. Natl. Acad. Sci.* 113, 12006–12011.
- 401 Duclaux, V., Caillé, F., Duez, C., Ybert, C., Bocquet, L., Clanet, C., 2007. Dynamics of transient

402 cavities. *J. Fluid Mech.* 591, 1–19.

403 Duez, C., Ybert, C., Clanet, C., Bocquet, L., 2007. Making a splash with water repellency. *Nat. Phys.* 3,  
404 180–183.

405 Dupeux, G., Goff, A. Le, Quéré, D., Clanet, C., 2010. The spinning ball spiral. *New J. Phys.* 12,  
406 093004.

407 Glasheen, J.W., McMahon, T.A., 1996. Vertical water entry of disks at low Froude numbers. *Phys.*  
408 *Fluids* 8, 2078–2083.

409 Grady, R.J., 1979. *Hydroballistics Design Handbook*, Naval Sea Systems command Hydromechanics  
410 Committee.

411 Grumstrup, T., Keller, J.B., Belmonte, A., 2007. Cavity ripples observed during the impact of solid  
412 objects into liquids. *Phys. Rev. Lett.* 99, 1–4.

413 Hirano, Y., Miura, K., 1970. Water impact accelerations of axially symmetric bodies. *J. Spacecr.*  
414 *Rockets* 7, 762–764.

415 Korobkin, A.A., Pukhnachov, V. V., 1988. Initial stage of water impact. *Annu. Rev. Fluid Mech.* 20,  
416 159–185.

417 Korobkin, A.A., Socolan, Y.M., 2006. Three-dimensional theory of water impact. Part 2. Linearized  
418 Wagner problem. *J. Fluid Mech.* 549, 343–373.

419 Lee, M., Longoria, R.G., Wilson, D.E., 1997. Cavity dynamics in high-speed water entry. *Phys. Fluids*  
420 9, 540–550.

421 May, A., 1975. *Water Entry and the Cavity-Running Behavior of Missiles*. Weapons Cent., White Oak  
422 Lab, MD. Tech. Rep. 20910, Nav. Surf.

423 Moghisi, M., Squire, P.T., 1981. An experimental investigation of the initial force of impact on a  
424 sphere striking a liquid surface. *J. Fluid Mech.* 108, 133–146.

425 Rosellini, L., Hersen, F., Clanet, C., Bocquet, L., 2005. Skipping stones. *J. Fluid Mech.* 543, 137–146.

426 Shiffman, M., Spencer, D.C., 1951. The force of impact on a cone striking a water surface (vertical  
427 entry). *Commun. Pure Appl. Math.* 4, 379–417.

428 Shiffman, M., Spencer, D.C., 1945. The force of impact on a sphere striking a water surface (second  
429 approximation). AMP Rep. 42.2R, AMG-NYU No. 133.

- 430 Speirs, N.B., Belden, J., Pan, Z., Holekamp, S., Badlissi, G., Jones, M., Truscott, T.T., 2019. The water  
431 entry of a sphere in a jet. *J. Fluid Mech.* 863, 956–968.
- 432 Thoroddsen, S.T., Etoh, T.G., Takehara, K., Takano, Y., 2004. Impact jetting by a solid sphere. *J.*  
433 *Fluid Mech.* 499, 139–148.
- 434 Truscott, T.T., Techet, A.H., 2009a. Water entry of spinning spheres. *J. Fluid Mech.* 625, 135–165.
- 435 Truscott, T.T., Techet, A.H., 2009b. A spin on cavity formation during water entry of hydrophobic and  
436 hydrophilic spheres. *Phys. Fluids* 21, 1–4.
- 437 Tveitnes, T., Fairlie-Clarke, A.C., Varyani, K., 2008. An experimental investigation into the constant  
438 velocity water entry of wedge-shaped sections. *Ocean Eng.* 35, 1463–1478.
- 439 Von Karman, T., 1929. The impact of seaplane floats during landing. Tech. Rep. 321. Natl. Advis.  
440 Comm. Aeronaut., Washington, DC.
- 441 Wagner, H., 1932. Phenomena associated with impacts and sliding on liquid surfaces. *J. Appl. Math.*  
442 *Mech.* 12, 193–215.
- 443 Wang, T.M., Yang, X.B., Liang, J.H., Yao, G.C., Zhao, W.D., 2013. CFD based investigation on the  
444 impact acceleration when a gannet impacts with water during plunge diving. *Bioinspiration and*  
445 *Biomimetics* 8, 036006.
- 446 Worthington, A.M., Cole, R.S., 1897. Impact with a Liquid Surface, Studied by the Aid of  
447 Instantaneous Photography. *Philos. Trans. R. Soc. A Math. Phys. Eng. Sci.* 189, 137–148.
- 448 Yu, Y.T., 1945. Virtual masses of rectangular plates and parallelepipeds in water. *J. Appl. Phys.* 16,  
449 724–730.
- 450
- 451 \* Corresponding author:
- 452 Chengchun Zhang<sup>a,b,\*</sup>, E-mail: [jluzcc@jlu.edu.cn](mailto:jluzcc@jlu.edu.cn)